Microsphere assistance in interference microscopy with high numerical aperture objective lenses

Lucie Hüser,* **Tobias Pahl, Marco Künne, and Peter Lehmann**
University of Kassel, EECS, Measurement Technology Group, Kassel, Germany

Abstract. Various attempts have been discussed to overcome the lateral resolution limit and thus to enlarge the fields of application of optical interference microscopy. Microsphere-assisted microscopy and interferometry have proven that the imaging of structures well below Abbe's resolution limit through near-field assistance is possible if microspheres are placed on the measured surface and utilized as near-field assisting imaging elements. The enhancement of the numerical aperture (NA) by the microspheres as well as photonic nanojets was identified to explain the resolution enhancement, but also whispering gallery modes and evanescent waves are assumed to have an influence. Up to now, to the best of our knowledge, there is no complete understanding of the underlying mechanisms and no model enabling to examine ideal imaging parameters. This contribution is intended to clarify how much the lateral resolution of an already highly resolving Linnik interferometer equipped with 100× NA 0.9 objective lenses can be further improved by microspheres. Our simulation model developed so far is based on rigorous near-field calculations combined with the diffraction-limited illumination and imaging process in an interference microscope. Here, we extend the model with respect to microsphere-assisted interference microscopy providing a rigorous simulation of the scattered electric field directly above the sphere. Simulation and experimental results will be compared in the three-dimensional spatial frequency domain and discussed in context with ray-tracing computations to achieve an in-depth understanding of the underlying mechanism of resolution enhancement by the microsphere. [DOI: 10.1117/1.JOM.2.4.044501]

Keywords: interference microscopy; microsphere assistance; resolution enhancement.

Paper 22014G received Jun. 13, 2022; accepted for publication Sep. 26, 2022; published online Oct. 28, 2022.

1 Introduction

Due to the ongoing trend toward miniaturization high-resolution optical imaging and three-dimensional (3D) microscopy is highly relevant in certain fields of science and technology. This is particularly true for interference microscopy, one of the most established techniques for micro- and nano-structure measurement. As the lateral resolution Λ_{min} follows the Abbe criterion

$$\Lambda_{\text{min}} = \frac{\lambda}{2\text{NA}}. \tag{1}$$

The conventional way of improving the lateral resolution capabilities of microscopes is to increase the numerical aperture $\text{NA} = n \sin \theta_{\text{max}}$ of the objective lenses and to reduce the wavelength λ of light. For air as the surrounding medium with the refractive index $n = 1$, the NA solely depends on the maximum angle θ_{max}, which is the maximum angle of incidence with respect to the optical axis and the maximum scattering or reflection angle that is captured by the microscope objective (MO) lens. In recent years, microsphere assistance has been proposed to improve the lateral resolution capabilities of conventional optical bright-field microscopes.[1] Furthermore, the use of microcylinders instead of microspheres has been reported.[2–4]

*Address all correspondence to Lucie Hüser, lucie.hueser@uni-kassel.de

A similar approach demonstrates what is called the super-resolving behavior of liquid-immersed microspheres[5] and points out the advantages compared to other resolution enhancement techniques.[6] Microsphere assistance was also successfully applied in context with confocal microscopy.[7] In addition, the illumination conditions with microsphere support and dark field microscopy were examined.[8,9]

More recently, microsphere assistance was also applied in white-light interference microscopy.[10] For phase-shifting interferometry, it was shown that with the support of near-field information provided by microspheres, it is possible to extend the resolution limit for interferometric height profile measurements.[11,12] NAs in the range of 0.3 to 0.85 were used, enabling access to high-frequency image information through the improvement of the optical resolution. Thus, high-spatial-frequency surface height information could be obtained by white-light and phase-shifting interferometers in both, Linnik as well as Mirau configurations.[13–15]

To explain the effect of the resolution enhancement, photonic nanojets are often referred to.[16–18] Their impact on resolution it is also discussed in detail by Darafsheh.[19] Nanojets describe the focus of light on the backside of a microsphere illuminated with a plane wave from the top. On the scale of microspheres, this focus is characterized by its high intensity and narrow waist.[20] Numerous papers have been published, studying the behavior and engineering of photonic nanojets.[21,22] Also, the role of evanescent waves and whispering gallery modes has been considered.[23,24] Detailed studies were also made on the resolution capabilities of Mie particles, which are in contact with the surface under investigation.[25] For further details it is referred to a recent review paper that gives an overview of the state-of-the-art in microsphere-assisted microscopy.[26]

Since incoherent Koehler illumination is applied in conventional bright-field and in interference microscopy, the microspheres are illuminated by multiple plane waves incident under various angles. Annular illumination of the outer region of microspheres turned out to affect the achieved resolution enhancement.[27,28] Nevertheless, until now there is no complete and widely accepted explanation of the resolution enhancement by microspheres in conventional microscopy and interferometry. For this reason, further analysis of the underlying physical principles is of predominant interest. Analyzing interference microscopes in the 3D spatial frequency domain by the 3D transfer function (TF) of the imaging system gives physical insight into the relevant transfer characteristics. Sheppard et al.[29] introduced a model, which represents the imaging process of confocal microscopes in the 3D spatial frequency domain. This model was applied in further publications to surface profile reconstruction in confocal microscopy[30,31] and later introduced as the foil model in coherence scanning interferometry (CSI).[32,33] We recently extended this model by treating the reference mirror in the same way as the object's surface[34] and pointed out the analogy with the 3D TF of a bright-field reflection microscope.[35] We further recognized that the transfer characteristics of 3D microscopes strongly depend on the scattering characteristics of the surface (single-point scatterers, mirror-like surfaces, or diffraction gratings) and the spectral characteristics of the light source.[36]

Analyzing the interferometric measurement data in the 3D spatial frequency domain, the influence of microspheres on the transfer behavior of the optical system could already be shown.[28,37,38] In the following, the transfer characteristics of a high-resolution Linnik interferometer with and without microsphere assistance are pointed out by 3D spatial frequency domain analysis of 3D image stacks of periodic grating structures. A comparison of the results exhibits that the transfer characteristics of microspheres described in the 3D frequency domain are closely related to the angular ranges of incident, reflected, and diffracted light rays. Thus, ray-tracing computations of light propagation through and inside the microsphere give further insight. Finally, experimental results obtained from gratings of different periods are compared to results of simulations based on rigorous finite element method (FEM) computations.

2 Experimental Setup

The Linnik interferometer sketched in Fig. 1(a) and displayed in Fig. 1(c) is used to record interference images at certain height positions during a depth scan. This results in the so-called

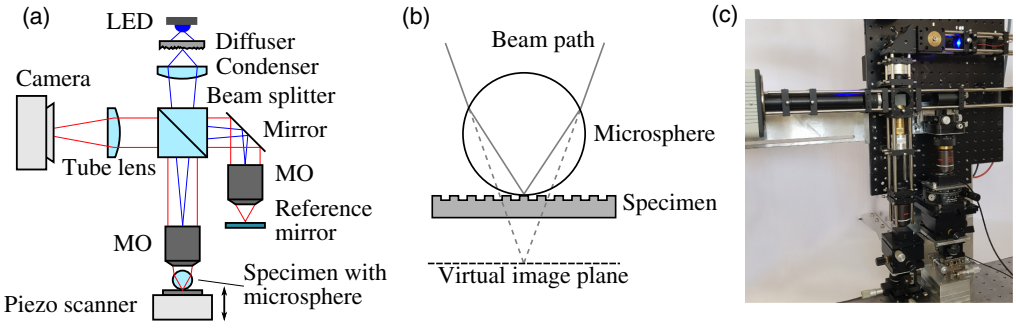

Fig. 1 (a) Scheme of the Linnik interferometer setup with the microsphere; (b) enlarged section showing a specimen with a microsphere on top creating a virtual image plane; and (c) photograph of the experimental setup in the laboratory.

3D image stack. Since our intention is to compare the resolution enhancement introduced by a microsphere in an already highly resolving microscope, we use two high-resolution MO lenses with 100× magnification and an NA of 0.9, which still provide a working distance of 1 mm. A scientific CMOS camera records the image stack. For illumination, a royalblue light-emitting diode emitting at a center wavelength of $\lambda = 440$ nm (Luxeon REBEL Color Line, spectral half-width 20 nm) arranged in a Koehler illumination setup and a transverse magnetic (TM) polarizer are utilized.

The depth scan is carried out using a precision piezo stage moving the object under investigation axially. Small height steps of typically 20 nm between two consecutive image frames are chosen to obtain a high number of sample points of the interference signals, which allows low-pass filtering to further reduce signal noise. The resulting image stack is analyzed pixel by pixel using envelope and phase evaluation algorithms to reconstruct the 3D topography of the surface.[39] It should be noted that the width of the envelope of the interference signals in this high NA Linnik interferometer configuration is dominated by the longitudinal spatial coherence of the focused light rather than the temporal coherence due to the spectral width of the blue LED. This effect is further described by Abdulhalim.[40]

When placing microspheres on the surface to be measured, these spheres are put on the object's surface in a liquid emulsion for practical reasons. After the liquid has evaporated, the measurement can be carried out. Throughout this study, SiO_2 microspheres with a diameter of 7 to 10 μm are being used. With the application of microspheres in the imaging path, an axial shift of the focus occurs and creates a virtual image plane as it is sketched in Fig. 1(b).

Our experiments included different diameters and materials of the spheres. It turned out that for MO lenses of high NA the number parameter combinations of microspheres suitable for microsphere-assisted interferometry is limited. For diameters larger than 20 μm, it was not possible to obtain a sharp image. Similar problems occurred at higher refractive indices. Based on these experimental results, a microsphere made of SiO_2 with relatively small diameters of 5 to 15 μm is a good choice for the high aperture experimental setup. However, there may be further parameter combinations working well too.

3 Analysis in the Spatial Frequency Domain

We assume the scattering geometry[41] according to Fig. 2(a), where $\mathbf{k}_{in}$ is the wave vector of a plane wave incident under an angle θ_{in}, and $\mathbf{k}_r$ and $\mathbf{k}_s$ are wave vectors of reflected and scattered waves propagating under the angles θ_r and θ_s, respectively. For a grating with a period Λ_{min} corresponding to the Abbe limit according to Eq. (1), the situation is outlined in Fig. 2(b). For the incidence angle $\theta_{in} = \theta_{max}$, the zeroth-order diffracted wave with wave vector $\mathbf{k}_r$ propagates under the angle $\theta_r = \theta_{max}$, whereas the scattering angle of the minus first-order diffracted wave is $\theta_s = -\theta_{max}$. The scattered electric field $U_s(\mathbf{q})$ under the Fraunhofer far-field condition can be calculated using the Kirchhoff formulation[29,41] with respect to a microscope in reflection mode assuming a perfectly reflecting surface $s(x, y)$ as

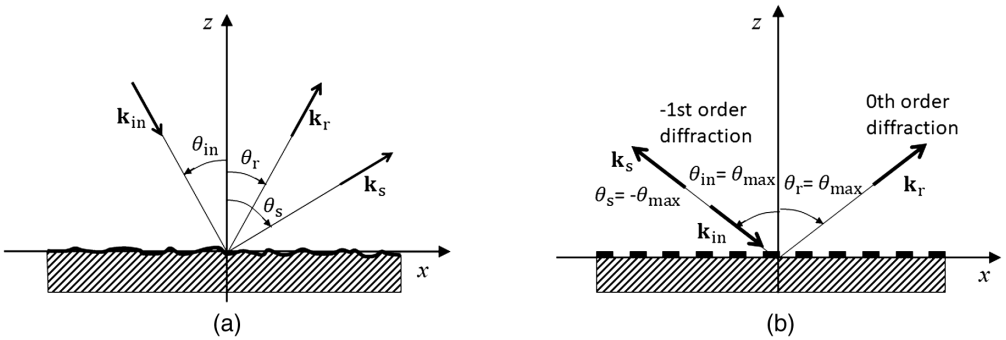

Fig. 2 Scattering geometry with (a) wave vectors of incident, reflected and scattered waves in the xz-plane and (b) wave vectors of reflected and -1st order diffracted wave vectors in xz-plane for a plane wave incident on a grating under the maximum angle θ_{max} restricted by the NA of a objective lens.

$$\begin{aligned} U_s(\mathbf{q}) &= \frac{1}{A}\int_A \mathrm{e}^{-\mathrm{i}(q_x x+q_y y+q_z s(x,y))}\mathrm{d}x\,\mathrm{d}y, \\ &= \frac{1}{A}\int_{-\infty}^{+\infty} A(x,y)\mathrm{e}^{-\mathrm{i}(q_x x+q_y y+q_z s(x,y))}\mathrm{d}x\,\mathrm{d}y, \\ &= \frac{1}{A}\mathcal{F}\{A(x,y)\} * \mathcal{F}\{\mathrm{e}^{-\mathrm{i}q_z s(x,y)}\}, \end{aligned} \tag{2}$$

where a monochromatic plane wave of wavelength λ and wavenumber $k_0 = 2\pi/\lambda$ is incident under the angle θ_{in}, and the vector $\mathbf{q} = \mathbf{k}_s - \mathbf{k}_{in}$ defines a point in the 3D Fourier domain. The scattered far-field $U_s(\mathbf{q})$ is normalized in a way that for a smooth surface and perpendicular incidence, i.e., $\theta_{in} = 0$, the amplitude in the specular direction becomes unity. The area $A(x, y)$ of integration in Eq. (2) corresponds to the field of view of the microscope, $\mathcal{F}\{\dots\}$ represents the Fourier transform, and $*$ the convolution symbol. $s(x, y) = s(x)$ applies for a surface textured in one dimension only. If the area A is large enough, Eq. (2) represents the two-dimensional (2D) Fourier transformation with respect to x and y of the phase object $\exp(-\mathrm{i}q_z s(x, y))$. If, for simplicity $s(x, y) = s(x)$ and considering wave vectors $\mathbf{k}_{in}$ and $\mathbf{k}_{in}$ only in the xz-plane, which then equals the plane of incidence and observation, the incident and scattered wave vectors are given as

$$\mathbf{k}_{in} = k_0 \begin{pmatrix} \sin\,\theta_{in} \\ 0 \\ -\cos\,\theta_{in} \end{pmatrix} \quad \text{and} \quad \mathbf{k}_s = k_0 \begin{pmatrix} \sin\,\theta_s \\ 0 \\ \cos\,\theta_s \end{pmatrix}. \tag{3}$$

Thus, the vector $\mathbf{q}$ results in

$$\mathbf{q} = \begin{pmatrix} q_x \\ q_y \\ q_z \end{pmatrix} = k_0 \begin{pmatrix} \sin\,\theta_s - \sin\,\theta_{in} \\ 0 \\ \cos\,\theta_s + \cos\,\theta_{in} \end{pmatrix}. \tag{4}$$

According to Eq. (4), the situation shown in Fig. 2(b) leads to

$$|q_x| = 2k_0\,\sin\,\theta_{max} = 2k_0\,\mathrm{NA} = \frac{2\pi}{\Lambda_{min}}. \tag{5}$$

The maximum lateral spatial frequency collected by a microscope lens of given NA value. Equation (5) is directly related to the Abbe resolution limit according to Eq. (1). The coordinates in $\mathbf{q}$-space follow the Ewald sphere construction shown in Fig. 3. Due to the NA of the microscope, the possible directions of the wave vectors of incident and scattered light are limited by the angle θ_{max}. According to Fig. 3(a), this results in the two spherical caps, which need to be correlated to calculate the 3D TF $H(\mathbf{q})$ of the instrument.[35] The outer boundary of the resulting

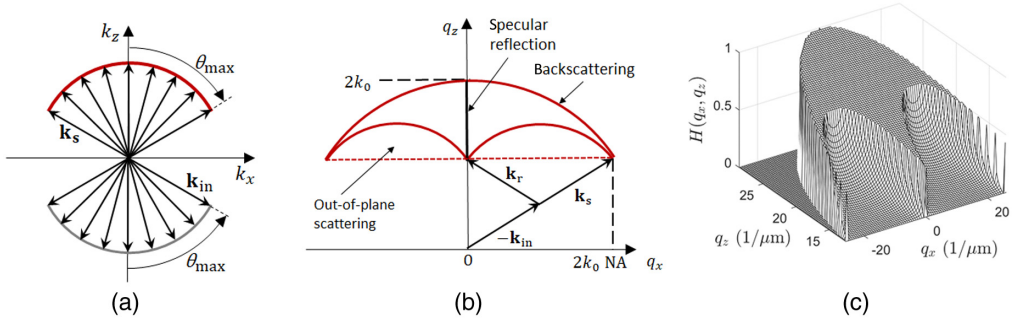

Fig. 3 (a) Ewald sphere construction based on two spherical caps defined by numerous wave vectors $\mathbf{k}_{in}$ and $\mathbf{k}_s$ with angles θ_{in} and θ_s below the maximum angle θ_{max} corresponding to the NA of the objective lens; (b) Ewald-limiting-sphere resulting from the correlation of the two caps; and (c) cross-section of the 3D TF for an interference microscope with NA = 0.9 and $\lambda = 440$ nm.[36]

Ewald-limiting-sphere is plotted in Fig. 3(b), where the contributions of the specular reflection are located on the q_z-axis and the outer spherical shell of radius $2k_0$ represents the back scattered light. It is worthy to note that the q_x-value is related to the spatial frequency component of a surface, whereas the corresponding q_z-values represent the spectral range of the corresponding interference signals. The whole construction shows rotational symmetry with respect to the q_z axis. Figure 3(c) shows a 2D cross sectional view in the q_xq_z-plane of $H(\mathbf{q})$, which holds for plane mirror-like surfaces and diffraction gratings.[36] Once $U_s(\mathbf{q})$ and $H(\mathbf{q})$ are known, the 3D spatial frequency representation of the interference intensity equals the product:

$$\Delta\tilde{I}(\mathbf{q}) = U_s(\mathbf{q})H(\mathbf{q}), \tag{6}$$

and the interference image stack $\Delta I(x, y, z)$ can be calculated via inverse 3D Fourier transform:

$$\Delta I(x, y, z) \sim \Re e\{\mathcal{F}^{-1}\{\Delta\tilde{I}(\mathbf{q})\}\}. \tag{7}$$

Cross sections of experimentally obtained spatial frequency representations $\Delta\tilde{I}(\mathbf{q})$ for different rectangular silicon phase gratings (RS-N standard by SiMETRICS) are shown in Fig. 4. Figure 4(a) shows the result for a rectangular grating of 6-μm period and 192-nm peak-to-valley (PV) amplitude, whereas Figs. 4(b) and 4(c) belong to gratings of 400 nm (b) and 300-nm period (c), both with a PV amplitude of 140 nm. The shape of the Ewald-limiting-sphere can be clearly recognized in Fig. 4(a). Figures 4(b) and 4(c) show only three diffraction orders, the zeroth order at $q_x = 0$ and the 1st and -1st orders, which are located at higher q_x values for the shorter period.

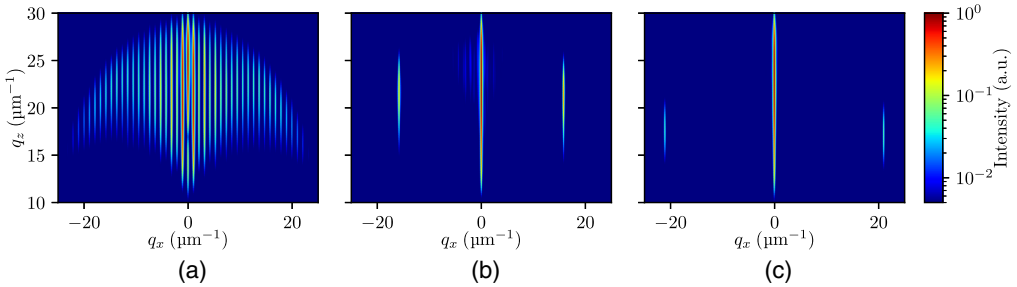

Fig. 4 Cross-section of the 3D spatial frequency representation of an interference image stack obtained without a microsphere for (a) a rectangular grating with 6-μm period and 192-nm height difference (RS-N standard by SiMETRICS); (b) a rectangular grating with 0.4-μm period and 140-nm height difference; and (c) a rectangular grating with 0.3-μm period and 140-nm height difference.

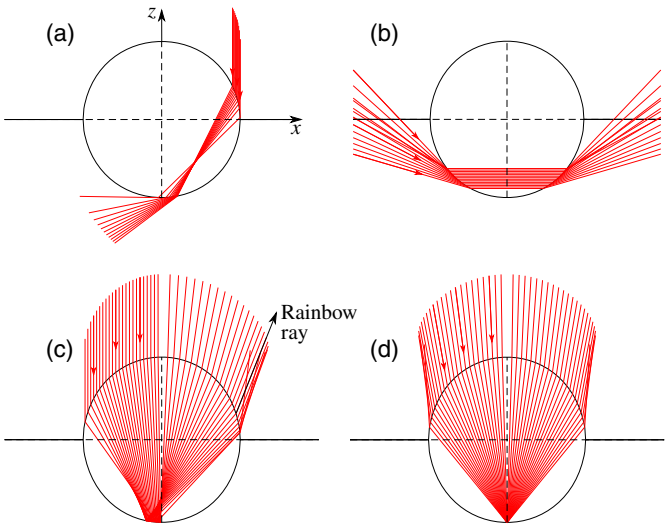

Fig. 5 Ray-tracing computations for a silica microsphere of refractive index $n_r = 1.4655$ at $\lambda = 440$ nm, (a) bundle of rays incident under an angle $\theta_{in} = 0$; (b) rays traveling horizontally through the microsphere; (c) internally reflected bundle of rays incident under an angle $\theta_{in} = 0$; and (d) incident rays internally reflected at the position $x = 0$, $z = -r$ inside the sphere.

4 Ray-tracing Results for a Microsphere

We already demonstrated experimentally that a phase grating with a minimum period length of 230 nm is resolved by the Linnik interferometer mentioned above in combination with microsphere assistance.[42] This period is slightly below the Abbe resolution limit of 244 nm, which holds for this interferometer without a microsphere. This section is intended to study, how light rays are refracted, reflected and focused by the microsphere to find out plausible mechanisms for the resolution enhancement. Since we use microspheres of at least 7-μm diameter ($r = 3.5$ μm), the Mie-parameter $2\pi k_0 r/\lambda$ is at least 50 and a physical description based on geometrical optics is a satisfying approximation to study basic effects.[43] Figure 5 shows some results of ray tracing computations assuming a microsphere of silica with a refractive index of 1.4655. In Fig. 5(a), a bundle of parallel light rays propagates along the vertical axis and hits the microsphere. The refracted light propagates through the microsphere, is refracted again and shows nearly grazing incidence with respect to a horizontal line located directly under the microsphere, where the object is typically placed. Due to the large angle of nearly 90 deg (defined with respect to the z-axis) of these rays refracted twice, the effective NA of the microsphere as an optical imaging element is close to unity. There are additional situations as shown in Figs. 5(b)–5(d), where the light never reaches a measuring object located underneath the microsphere. These ray paths lead to additional interference components although they are not affected by the surface of the measuring object. In Fig. 5(b), the incident light rays show a relatively large angle of incidence with respect to the z-axis. However, all angles are below the maximum angle θ_{max} defined by the NA of the system. The rays travel horizontally through the microsphere. Due to the symmetry of the arrangement the scattering angle equals the angle of incidence, i.e. $\theta_s = \theta_{in}$. Hence, for these rays $q_x = 0$ and the corresponding q_z-values are relatively small. In Fig. 5(c), parallel rays are incident on the left hand side. These rays are refracted at the boundary of the microsphere and are then internally reflected at the bottom of the sphere. After an additional refraction, they propagate in air and include relatively small angles with the z-axis, thus the corresponding q_x-values are low and q_z-values high. This is the arrangement belonging to the rainbow and, indeed, the rainbow ray[43] can be identified as the ray on the right hand side, which corresponds to the maximum scattering angle. The rays close to the rainbow ray form a caustic, and thus, in these regions high intensity values occur. A similar situation is shown in Fig. 5(d), which shows symmetry with respect to the z-axis, since all rays are internally reflected at the coordinate $x = 0$, $z = -r$ inside the microsphere and, therefore, $q_x = 0$ for these rays. Figure 5(d) demonstrates that the

incident and scattered rays again include rather small angles with the z-axes, such that no total internal reflection inside the microsphere occurs. Light incident at higher angles is no longer reflected at $x = 0$, $z = -r$. Therefore q_z is quite high for the rays plotted in Fig. 5(d).

5 Experimental Results

The interferometric measurement data is acquired through a stepwise depth scan with a step height of 20 nm performed by a piezo scanner. This results in a measuring process known from CSI, however, additionally utilizing microsphere assistance. The measurement object is the RS-N resolution standard by SiMETRICS. Mainly the 300- and 600-nm grating structures with nominal depths of 140 and 160 nm, respectively, are examined.

While performing CSI measurements, the height information of the specimen's surface is encoded in the phase of the interference signals. To gain a better understanding of the phase modulation occurring in interferometric measurement, xz-cross sections of (offset-free) interference images acquired through a depth scan are shown in Fig. 6. The results shown in Figs. 6(a) and 6(b) are obtained from the 300- and 600-nm grating structure of the RS-N standard using microsphere assistance, i.e., placing a microsphere directly on the grating structure. For comparison, Fig. 6(c) shows how the image stacks recorded for a mirror instead of a grating leads to highest contrast of the modulation in z-direction of the interference signals centered around the virtual image plane. It is worthy to note that the position on the z-axis is related to the range of the depth scan, which is typically 5- to 10-μm long. The virtual image plane is placed approximately in the middle of this range and $z = 0$ denotes the starting position of the scan range. In x-direction, the phase modulation introduced by the surface of the measured grating structures is visible in Figs. 6(a) and 6(b). The interference signals can be analyzed using envelope- and phase retrieving algorithms to reconstruct the grating structure of the object as previously shown.[42] In addition, the resolution enhancement through the imaging process also an additional magnification is introduced by the microspheres.

For comparability with the results shown in Secs. 3 and 4, the spatial frequency domain representation of the interference data is analyzed as introduced beforehand. First, the data are preprocessed by means of Blackman-windowing as well as zero-padding to exclude contributions occurring besides the microsphere and to improve the spatial frequency resolution, respectively. The data are further offset reduced. Cross sections of the spatial frequency representation in the $q_x q_z$-plane are shown in Fig. 7 accordingly.

As it is shown in Eq. (5) and illustrated in Fig. 4, for a one-dimensional grating structure imaged by an interference microscope, the diffraction orders are visible as corresponding sharp lines at $q_x = \text{const.}$ in the 3D spatial frequency representation. The additional magnification factor introduced by the microsphere was determined to be $M = 1.4$ for our setup. Thus, for the grating of 300-nm period the q_x-value corresponding to the first-order diffraction maximum is shifted by the mircosphere from $q_{x,a} \approx \pm 21\ \mu\text{m}^{-1}$ in Fig. 4(c) to $q_{x,a} \approx \pm 15\ \mu\text{m}^{-1}$ according to Fig. 7(a), since the period length Λ is multiplied by M. Consequently, the 600-nm grating

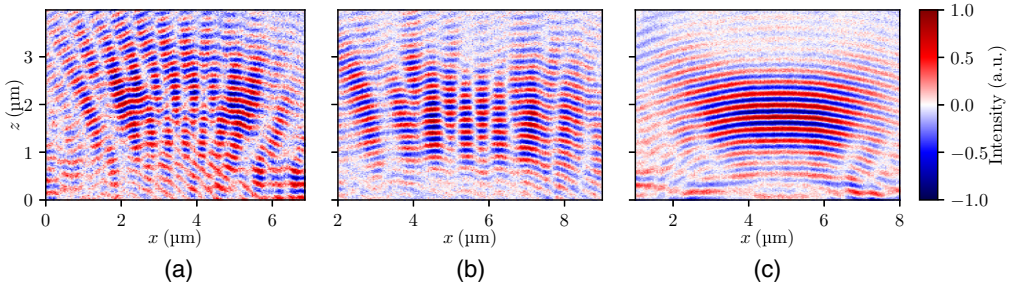

Fig. 6 xz-cross sections of offset-reduced interference image stacks acquired with microsphere assistance via a depth scan using royal blue illumination of rectangular silicon gratings (RS-N standard) with period lengths of (a) 300 nm; (b) 600 nm; and (c) a mirror surface for comparison.

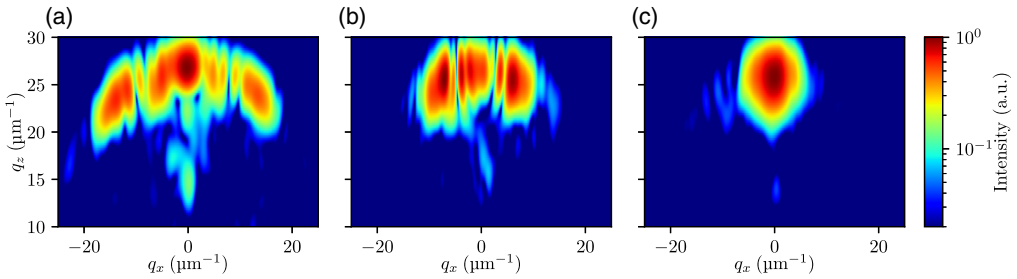

Fig. 7 $q_x q_z$-cross-sections of 3D spatial frequency representations of the interference image stacks corresponding to (a) the 300-nm grating structure; (b) the 600-nm grating; and (c) the mirror surface.

magnified by the microsphere leads to first-order diffraction maxima at $q_{x,a} \approx \pm 7.5\ \mu\text{m}^{-1}$ as it is displayed in Fig. 7(b). Finally, for the mirror no diffraction order except for the zero-order located at $q_x = 0$ appears, as shown in Fig. 7(c).

Further, the transfer behavior of the microsphere-assisted setup differs compared to an interference microscope without a microsphere. The size of the field of view limited by the microsphere significantly influences the intensity distribution in the 3D spatial frequency domain. According to Eq. (2), the field of view corresponds to the area of integration described by $A(x, y)$. This leads to a convolution in the 3D spatial frequency domain of the diffraction pattern of the grating with an Airy-disk function (implying a circular shaped field of view). The smaller the field of view $A(x, y)$ the broader is this Airy-disk and the corresponding blurring of the diffraction maxima. As stated by Sheppard,[44] broadening of diffraction orders due to a small field of view has a significant influence on the resolution capabilities of a system. Due to optical aberrations introduced by the microsphere and the Blackman window used to extract the relevant lateral and axial range in the spatial domain, the frequency response is additionally affected. As a result, a broadening of the discrete intensity pattern, i.e., the sharp lines at certain q_x-values initiated by diffraction at the grating structure, occurs. This becomes apparent by comparison of Figs. 7(a), 7(b) and 4. In addition, the light diffracted by the grating, additional intensity contributions in Fig. 7 can be attributed to the microsphere itself, e.g., the intensity maximum at $q_x = 0$, $q_z \approx 15\ \mu\text{m}^{-1}$, which corresponds to the situation according to Fig. 5(b) and the higher frequency rippling, which is a consequence of the increased scattered light intensity under the rainbow angle shown in Fig. 5(c).

6 Rigorous Simulations

To investigate further influences on the transfer behavior of the microspheres as well as the influence of photonic nanojets, rigorous simulations were performed, which are presented in the following.

6.1 *Simulation of the Complete Imaging Process*

The measured data are compared to simulation results of the imaging process, where the light-surface interaction considering the microsphere is based on rigorous FEM computation of the electric field distribution. The transfer characteristics of the interference microscope as well as the phase shifts introduced by the depth scan are considered by filter operations using Fourier optics modeling. The combined model enables a full 3D simulation of illumination and diffraction at 2D periodic surfaces and provides accurate results compared with CSI measurements.[45,46] In this study, the model is extended considering a microsphere with a radius of $r = 2.5\ \mu\text{m}$ and a refractive index of $n = 1.5$, which is placed directly on the specimen. For computational reasons, microspheres are arranged in a periodic manner with a period length $L_x = 13.2\ \mu\text{m}$. Due to computational and time constraints, the simulation is performed on 2D surface structures and the microsphere is approximated by a microcylinder, as cylindrical microelements were shown to

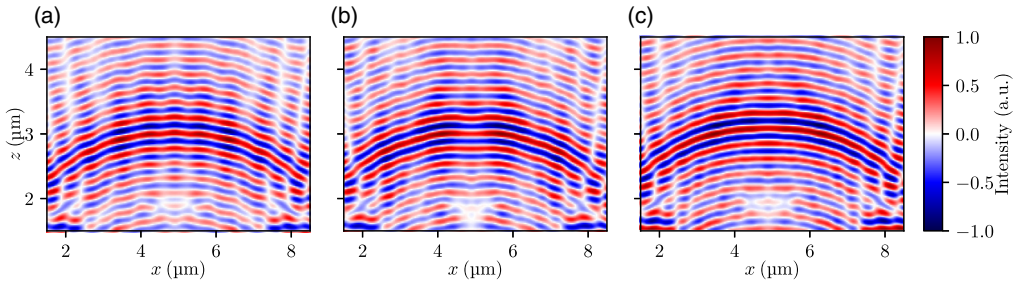

Fig. 8 *xz*-cross sections of offset-reduced interference image stacks obtained by rigorous simulation.[46] The periods of the underlying sinusoidal grating structure of 25-nm PV amplitude correspond to the RS-N resolution standard with period length of (a) 300; (b) 600 nm; and (c) results of a flat mirror surface for comparison.

enhance the lateral resolution capabilities too.[4,47,48] Since we are interested in general effects of microsphere-induced resolution enhancement, it is reasonable not to use exactly the same configuration for measurement and simulation.

With respect to Koehler illumination, it can be assumed that the illumination of the specimen is composed of individual incoherent partial plane waves. These illuminate the specimen from all angles which cover the aperture of the objective. To realize the conical illumination, discretization is performed over these angular values and rigorous simulations of the near field are conducted using plane wave illumination for each discrete incident angle. For each simulated near field, the far-field expansion and Fourier optics modeling of the imaging processes in the microscope are performed. Afterwards, the interference intensity distribution considering the reference field is calculated for each set of incident angles and the final incoherent summation of the results is done.[46]

Figure 8 shows extracts of offset reduced interference image stacks in the presence of a microsphere simulated with TM polarized monochromatic light of $\lambda = 440$ nm and NA $= 0.9$. Due to the high NA value, the light source can be assumed as monochromatic, since the influence of temporal coherence is negligible for single-colored LEDs. The underlying structure is a sinusoidal grating with PV height of 25 nm and period lengths corresponding to those of the measured results shown in Fig. 6. To avoid additional effects such as multiple scattering and edge diffraction, the height is chosen to be smaller compared to the measured profile.

Considering Figs. 6 and 8, significant key characteristics can be compared. In both figures, the grating structure appears in the phase modulation of the interference signals. For the experimental results, the phase modulation is more pronounced in amplitude, since a rectangular grating (RS-N standard) was used. Similar to the measurement result, the simulated interference signals obtained from a flat mirror [Fig. 8(c)] do not show a grating-dependent lateral phase modulation. Detailed comparison of simulated and measured results exhibits deviations. These are mainly due to the fact that results measured using a sphere are compared to simulation results obtained from a cylinder because of the computational effort mentioned above. Further, the sphere is arbitrarily placed on the grating and thus at different positions with respect to the grating structure in simulations. Additionally, the spheres have a different radius compared to the cylinder leading to further deviations. Nevertheless, the qualitative comparison between simulated and experimental results demonstrates that in principle the simulation model reflects the relevant physical mechanisms in microsphere-assisted interferometry.

To analyze the interference signals in more detail, Fig. 9 shows the representation in $\boldsymbol{q}$-space. Comparing simulation and measurement results, the diffraction orders are blurred in the measurement results. The intensity obtained from a plane mirror [Fig. 9(c)] shows an additional periodic modulation of the intensity distribution for larger q_z and small q_x values. This is probably a consequence of the rainbow effect explained in Sec. 4, since further simulation results turn out that the modulation period behaves anti-proportional to the microsphere's diameter. This phenomenon is not as clearly observed in the measurement results obtained from a plane mirror, but the differences can be explained by the use of microcylinders in the simulation instead of spheres.

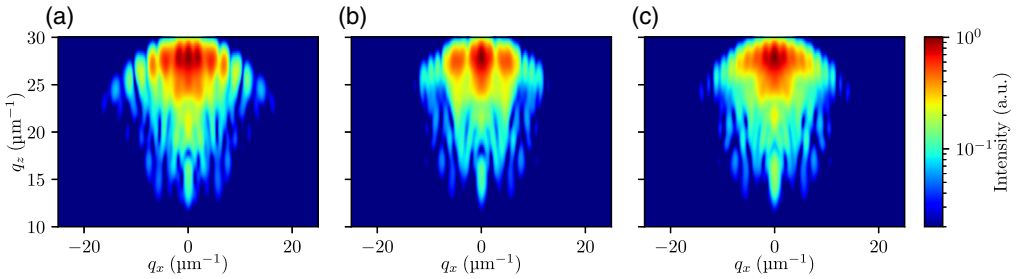

Fig. 9 $q_x q_z$-cross-sections of 3D spatial frequency representations of the simulated interference image stacks corresponding to (a) the 300-nm sinusoidal grating; (b) the 600-nm grating; and (c) the mirror surface.

However, a slight modulation can be observed even in the measurement results, especially in the case of Figs. 7(a) and 7(b). It is worthy to note that due to the sinusoidal grating structure with a relatively low PV amplitude of 25 nm, the intensity of the blurred diffraction orders is not as pronounced as in the measurement results. Furthermore, in both, measurement and simulation, an intensity contribution at $q_x = 0$ for small values of q_z is visible with and without a grating structure. This can be assigned to the rays traveling horizontally through the microcylinder as it is shown in Fig. 5(b) and confirmed by simulations assuming a microcylinder in free space. The high intensity for large q_z values and $q_x \approx 0$ follow from the rays depicted in Fig. 5(d), where rays of oblique incidence and scattering angles inside the sphere are refracted such that above the sphere smaller angles and hence larger values of q_z result.

In sum, the rigorous simulation model reproduces the major effects occurring in measurement results. Artefacts observed in the 3D spatial frequency domain can be assigned to general cases of ray tracing. Thus, the **q**-space representation is shown to be quite useful to analyze the physical mechanism introduced by microspheres. Furthermore, diffraction orders belonging to the measured grating structure under the sphere lead to smaller q_x and larger q_z values due to the magnification of the sphere as supposed by Hüser and Lehmann.[28,42] This effect is now confirmed by simulations of grating structures of different period.

6.2 *Studies on Photonic Nanojets*

Rigorous simulations were performed to study the influence of photonic nanojets. In this case, the results are obtained with 2D FEM simulations of the electromagnetic field distribution. Only perpendicular incidence of a monochromatic plane wave under an angle $\theta_{\text{in}} = 0$ is considered ($\lambda = 440$ nm). The phenomenon of photonic nanojets occurring on the back surface of microspheres or microcylinders was widely studied.[19,49] However, these investigations do not include the configuration of an interferometer in reflection mode as it is studied here. Therefore, an additional simulation with a microcylinder on a grating (period length 300 nm) is carried out. The intensity distributions obtained with and without the grating are shown in Fig. 10.

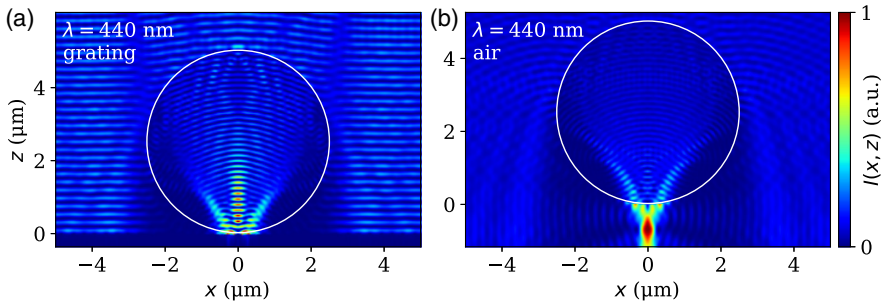

Fig. 10 Simulation results for a microcylinder illuminated by a monochromatic plane wave for the cases (a) with a diffraction grating (300-nm period length) directly below the cylinder and (b) in air surrounding.

When comparing the results from Figs. 10(a) and 10(b), the photonic nanojet obviously disappears for the case of the grating located directly below the microcylinder. The specimen is placed at the location, where the nanojet in air occurs. Hence, the generation of a nanojet will be disturbed, and instead, an interaction of the corresponding electromagnetic waves with the specimen's surface takes place. Furthermore, the case of near grazing incidence below the microcylinder shown in Fig. 5(a) arises. The light diffracted from the grating can contribute to the imaging process and thus high aperture imaging occurs even if MO lenses of low NA are used.

7 Discussion

To analyze the resolution enhancement, we compare both, experimental and simulated interference image stacks in the spatial and the three-dimensional spatial frequency domain. This methodology provides advantages as it explains the occurring phenomena based on light rays traveling under different angles with respect to the optical axis and thus enables comparisons with ray-tracing computations and rigorous simulations as well. In 3D Fourier space effects occurring through the microsphere itself independently of the specimen can be separated from effects introduced by the interaction of light and the specimen via the microsphere. Microspheres shift the intensity diffraction maxima of a grating to lower spatial frequencies. As a consequence, the central wavelength of the resulting interference signals is significantly reduced if microspheres are used. In combination with ray-tracing and rigorous simulation results, we conclude that the most dominant effect, which arises from the microspheres, can be viewed as an effective enlargement of the NA of the optical system.

8 Conclusion

Although microsphere-assisted resolution enhancement is frequently used in optical imaging and 3D microscopy, the physical mechanism behind this phenomenon is still not completely understood. The most frequently mentioned explanation attempts refer to the enhancement of the NA, the collection of evanescent waves, the photonic nanojet effect, and the excitation of whispering gallery modes.

The methodologies presented in this article can be applied to several configurations of microsphere-assisted interferometry and microscopy. Analysis in the 3D spatial frequency domain gives valuable insight into the transfer behavior of optical systems with different NA and other optical properties.

The rigorous simulation model represents a complete computational approach of the imaging process through the microsphere. This method enables a more specific look on relevant mechanisms responsible for the transfer behavior of microsphere-assisted interferometry. With this model, e.g., the influences of whispering gallery modes and evanescent waves on the imaging process can be elaborated further.

Since we use 3D microscopy in reflection mode, we suppose direct reflection and diffraction of propagating waves to be dominant and thus implications of evanescent waves and whispering gallery modes to be negligible. Therefore, our investigation suggests that the most likely mechanism is the enhancement of the NA, which is close to 1 in case of microsphere assistance, in combination with the rather limited field of view under the microsphere. The fact that higher magnifications than $M = 1.4$ could not be obtained with our experimental configuration is one of the facts that led us to conclude that the numerical aperture must be increased effectively by the microsphere and finally limits the resolution of microsphere-based interferometry. For our microscope with an NA of 0.9 a resolution enhancement of 11% is achieved using microspheres. Since the occurrence of photonic nanojets also relies on the coherent superposition of waves propagating under higher angles with respect to optical axis the physical origins of nanojets and NA enhancement are closely related to each other.

Acknowledgments

The partial support of this project by the DFG (German Research Foundation) (Grant No. LE992/15-1) is gratefully acknowledged.

References

1. Z. Wang et al., "Optical virtual imaging at 50 nm lateral resolution with a white-light nanoscope," *Nat. Commun.* **2**(1), 1–6 (2011).
2. A. Darafsheh, Y. Li, and V. N. Astratov, "Super-resolution microscopy by dielectric microcylinders," in *Int. Conf. Transparent Opt. Netw.*, pp. 100–102 (2013).
3. A. Darafsheh and D. Bollinger, "Systematic study of the characteristics of the photonic nanojets formed by dielectric microcylinders," *Opt. Commun.* **402**, 270–275 (2017).
4. J. N. Monks et al., "Spider silk: mother nature's bio-superlens," *Nano Lett.* **16**(9), 5842–5845 (2016).
5. A. Darafsheh et al., "Optical super-resolution by high-index liquid-immersed microspheres," *Appl. Phys. Lett.* **101**(14), 141128 (2012).
6. A. Darafsheh et al., "Advantages of microsphere-assisted super-resolution imaging technique over solid immersion lens and confocal microscopies," *Appl. Phys. Lett.* **104**(6) (2014).
7. Y. Yan et al., "Microsphere-coupled scanning laser confocal nanoscope for sub-diffraction-limited imaging at 25 nm lateral resolution in the visible spectrum," *ACS Nano* **8**, 1809–1816 (2014).
8. S. Perrin et al., "Illumination conditions in microsphere-assisted microscopy," *J. Microsc.* **274**(1), 69–75 (2019).
9. S. Perrin et al., "Transmission microsphere-assisted dark-field microscopy," *Phys. Status Solidi - Rapid Res. Lett.* **13**(2), 1800445–4 (2019).
10. F. Wang et al., "Three-dimensional super-resolution morphology by near-field assisted white-light interferometry," *Sci. Rep.* **6**(1), 24703 (2016).
11. S. Perrin et al., "Microsphere-assisted phase-shifting profilometry," *Appl. Opt.* **56**(25), 7249–7255 (2017).
12. A. Leong-Hoi et al., "High resolution microsphere-assisted interference microscopy for 3D characterization of nanomaterials," *physica. status solidi. (a)* **215**(6), 1700858 (2018).
13. P. C. Montgomery et al., "Sub-diffraction surface topography measurement using a microsphere-assisted Linnik interferometer," *Proc. SPIE* **10329**, 1032918 (2017).
14. P. Montgomery et al., "3D nano surface profilometry by combining the photonic nanojet with interferometry," *J. Phys.: Conf. Ser.* **794**(1), 012006 (2017).
15. I. Kassamakov et al., "3D super-resolution optical profiling using microsphere enhanced mirau interferometry," *Sci. Rep.* **7**(1), 1–7 (2017).
16. H. Yang et al., "Super-resolution imaging of a dielectric microsphere is governed by the waist of its photonic nanojet," *Nano Lett.* **16**(8), 4862–4870 (2016).
17. A. Maslov and V. Astratov, "Resolution and reciprocity in microspherical nanoscopy: point-spread function versus photonic nanojets," *Phys. Rev. Appl.* **11**(6), 064004 (2019).
18. B. S. Luk'yanchuk et al., "Refractive index less than two: photonic nanojets yesterday, today and tomorrow [Invited]," *Opt. Mater. Express* **7**(6), 1820 (2017).
19. A. Darafsheh, "Photonic nanojets and their applications," *J. Phys.: Photonics* **3**(2), 022001 (2021).
20. A. Heifertz et al., "Photonic nanojets," *J. Comput. Theor. Nanosci.* **6**(9), 1979–1992 (2009).
21. C. Rockstuhl et al., "Engineering photonic nanojets," *Opt. Express* **19**(11), 10206 (2011).
22. M. S. Kim et al., "Gouy phase anomaly in photonic nanojets," *Appl. Phys. Lett.* **98**(19), 191114 (2011).
23. S. Zhou et al., "Effects of whispering gallery mode in microsphere super-resolution imaging," *Appl. Phys. B: Lasers Opt.* **123**(9), 1–9 (2017).
24. Y. Ben-Aryeh, "Increase of resolution by use of microspheres related to complex Snell's law," *J. Opt. Soc. Am. A* **33**(12), 2284 (2016).
25. A. V. Maslov and V. N. Astratov, "Optical nanoscopy with contact Mie-particles: resolution analysis," *Appl. Phys. Lett.* **110**, 261107 (2017).
26. A. Darafsheh, "Microsphere-assisted microscopy," *J. Appl. Phys.* **131**(3), 031102 (2022).
27. M. X. Wu et al., "Modulation of photonic nanojets generated by microspheres decorated with concentric rings," *Opt. Express* **23**(15), 20096 (2015).
28. L. Hueser and P. Lehmann, "Analysis of resolution enhancement through microsphere-assisted interferometry in the 3D spatial frequency domain," *Proc. SPIE* **11782**, 117820R (2021).

29. C. J. Sheppard, T. J. Connolly, and M. Gu, "Imaging and reconstruction for rough surface scattering in the Kirchhoff approximation by confocal microscopy," *J. Mod. Opt.* **40**(12), 2407–2421 (1993).
30. J. C. Quartel and C. J. Sheppard, "A surface reconstruction algorithm based on confocal interferometric profiling," *J. Mod. Opt.* **43**(3), 591–605 (1996).
31. J. C. Quartel and C. J. Sheppard, "Surface reconstruction using an algorithm based on confocal imaging," *J. Mod. Opt.* **43**(3), 469–486 (1996).
32. J. Coupland et al., "Coherence scanning interferometry: linear theory of surface measurement," *Appl. Opt.* **52**(16), 3662–3670 (2013).
33. R. Su et al., "Scattering and three-dimensional imaging in surface topography measuring interference microscopy," *J. Opt. Soc. Am. A* **38**(2), A27 (2021).
34. P. Lehmann, M. Künne, and T. Pahl, "Analysis of interference microscopy in the spatial frequency domain," *J. Phys.: Photonics* **3**, 014006 (2021).
35. P. Lehmann and T. Pahl, "Three-dimensional transfer function of optical microscopes in reflection mode," *J. Microsc.* **284**, 45–55 (2021).
36. P. Lehmann, S. Hagemeier, and T. Pahl, "Three-dimensional transfer functions of interference microscopes," *Metrology* **1**(2), 122–141 (2021).
37. L. Hüser and P. Lehmann, "Microsphere-assisted interference microscopy for resolution enhancement," *Technisches Messen* **88**(5), 311–318 (2021).
38. L. Hüser et al., "The use of microsphere assistance in interference microscopy with high numerical aperture objective lenses," *Proc. SPIE* **12152**, 1215204 (2022).
39. S. Tereschenko, "Digitale analyse periodischer und transienter Messsignale anhand von Beispielen aus der optischen Präzisionsmesstechnik," PhD thesis, Universität Kassel (2018).
40. I. Abdulhalim, "Spatial and temporal coherence effects in interference microscopy and full-field optical coherence tomography," *Annalen der Physik* **524**(12), 787–804 (2012).
41. P. Beckmann and A. Spizzichino, *The Scattering of Electromagnetic Waves from Rough Surfaces*, Artech House Inc., Norwood (1987).
42. L. Hüser and P. Lehmann, "Microsphere assisted interferometry with high numerical apertures for 3D topography measurements," *Appl. Opt.* **59**(6), 1695–1702 (2020).
43. H. C. van de Hulst, *Light Scattering by Small Particles*, Dover Publications, Inc (1981).
44. C. J. R. Sheppard, "Resolution and super-resolution," *Microsc. Res. Tech.* **80**, 590–598 (2017).
45. T. Pahl et al., "Two-dimensional modelling of systematic surface height deviations in optical interference microscopy based on rigorous near field calculation," *J. Mod. Opt.* **67**(11), 963–973 (2020).
46. T. Pahl et al., "3D modeling of coherence scanning interferometry on 2D surfaces using FEM," *Opt. Express* **28**(26), 39807 (2020).
47. A. Darafsheh, "Optical super-resolution and periodical focusing effects by dielectric microspheres," PhD thesis, The University of North Carolina at Charlotte (2013).
48. A. Darafsheh et al., "Super-resolution optical microscopy by using dielectric microwires," *Proc. SPIE* **9713**, 97130U (2016).
49. Z. Chen, A. Taflove, and V. Backman, "Photonic nanojet enhancement of backscattering of light by nanoparticles: a potential novel visible-light ultramicroscopy technique," *Opt. Express* **12**(7), 1214 (2004).

Lucie Hüser has been working as a research assistant and a PhD candidate in the Measurement Technology Group, Department of Electrical Engineering and Computer Science at the University of Kassel since 2018. She received her master's degree in electrical engineering in 2017 at the University of Kassel. Her main research areas are interference microscopes with high NAs and near-field support in interference microscopy.

Tobias Pahl received his master's degree in physics in 2018 at the University of Münster. He has been working as a research assistant and PhD candidate in the Measurement Technology Group, Department of Electrical Engineering and Computer Science at the University of Kassel since 2019. His main research interests are interference and confocal microscopes with high NAs and their modeling.

Marco Künne is a research assistant in the measurement technology group of the University of Kassel, faculty of Electrical Engineering and Computer Science Department. He studied nanoscience at the University of Kassel until 2019. He is working in the research field of high-resolution optical interferometry.

Peter Lehmann studied physics at the Universities of Münster and Karlsruhe. He reached the Dr.-Ing. degree at the University of Bremen in 1994 and finished his Habilitation in 2002. From 2001 until 2008, he was employed at an industrial manufacturer of measuring instruments, where he coordinated research activities in optical metrology. Since then he is a full professor (W3) and holds the chair in measurement technology at the faculty of electrical engineering and computer science of the University of Kassel, Germany. His research interests relate especially to interferometric methods in optical metrology.